CrossMark

Numerically simulating impact disruptions of cohesive glass bead agglomerates using the soft-sphere discrete element method

Stephen R. Schwartz [a,b,*], Patrick Michel [b], Derek C. Richardson [a]

[a] Department of Astronomy, University of Maryland, College Park, MD 20740-2421, United States
[b] Lagrange Laboratory, University of Nice Sophia Antipolis, CNRS, Observatoire de la Côte d'Azur, B.P. 4229, 06304 Nice Cedex 4, France

ARTICLE INFO

ABSTRACT

We present our implementation of cohesion in the parallel N-body code pkdgrav in order to model small bodies that are not fully monolithic but that have at least some degree of cohesion. Small bodies of our Solar System show a great diversity in shapes, sizes and morphologies. However, we do not have direct information on their internal structure. The response of small bodies to various kinds of processes, such as impacts, depends on their internal properties in a way that is not yet well understood. It is therefore important to model the different kinds of structures that can represent a small body, and to study their influence on the way a body responds to the different processes undergone during its lifetime. Here, we present a preliminary study to serve as validation of our implementation of cohesive forces into pkdgrav. This study consists of comparing low-speed laboratory impact experiments on sintered glass bead agglomerates from a previously published work against our numerical simulations, which replicate those impact conditions. The experimental targets are numerically modeled as agglomerates of soft spheres bound together by spring-like forces that mimic their cohesion. First we check that the strength properties of the numerical target are identical to the real ones by successfully modeling numerically the Brazilian disk test, a standard experimental test to measure the tensile strength of various kinds of materials. We then reproduce in simulation two experiments that were performed using different impact conditions. The numerical results show that the outcome is very sensitive to the exact location of the impact point, as observed in experiments, and we find, in each case, satisfying agreement with experimental outcomes. This gives us confidence that we can apply our model in future studies to low-speed collisions between aggregates, as occurred during the early phases of our Solar System's history, and investigate a wide range of parameter space (e.g., material properties such as cohesion) as well as target shapes and/or sizes of individual spherical components, and the influence of the initial target rotation. Also in future studies will also apply our model to other processes such as rotational fragmentation of cohesive aggregates resulting from YORP spin-up.

© 2013 Elsevier Inc. All rights reserved.

1. Introduction

In this paper, we present the implementation of cohesion into a numerical model aimed at the study of the dynamics of granular materials that comprise the surfaces and, in some cases, the interiors of small Solar System bodies. For validation, we simulate impact experiments into small targets of sintered spherical glass bead agglomerates.

Space mission images of small bodies have shown a great diversity of shapes, sizes, and morphologies. Moreover, the bulk densities that have been measured for some of these small bodies suggest that their internal structure contains some degree of porosity, as the values are systematically smaller than the bulk densities of meteoritic analogues (Consolmagno et al., 2008). For instance, the NEAR-Shoemaker spacecraft performed a fly-by of the Asteroid (253) Mathilde in 1997, which allowed the determination of the bulk density of this C-type asteroid (Yeomans et al., 1997). Its value is about 1.35 g/cm^3, which suggests a porosity fraction up to 40% when compared to the bulk density of carbonaceous chondrites. Both observational and numerical works suggest that a large fraction of small bodies, possibly down to a few hundreds of meters in size, consist of rubble piles, whose strength is dominated by self-gravity (e.g., Benz and Asphaug, 1999). However, such gravitational aggregates may also contain some cohesion, with the smaller components of the small-body population likely dominated by cohesion, since these typically spin too fast to be able to retain their shape if gravity alone were the only source of strength (Holsapple, 2007).

* Corresponding author at: Department of Astronomy Computer and Space Sciences Building, Stadium Drive, University of Maryland, College Park MD 20742-2421, United States. Fax: +1 301 314 9067.
E-mail address: srs@astro.umd.edu (S.R. Schwartz).

Our knowledge of the internal makeup of small bodies is still very poor; the response of small bodies to various kinds of influences—processes such as impacts or shaking—depends on their surface and/or internal properties in a way that is not yet well understood. In turn, such processes can then modify this makeup. Since we do not have precise knowledge of either, it is important to create models that can represent small bodies in order that we are able to study the influence of different properties on the way a body may respond to the different processes it undergoes during its lifetime. We recently adapted the parallel *N*-body code PKDGRAV to the modeling of the evolution of the granular materials that may comprise the surface and the inside of small bodies (see Richardson et al., 2011; Schwartz et al., 2012). In particular, bodies that are not fully monolithic, but instead have at least some degree of cohesion, may be represented as gravitational aggregates composed of solid blocks linked together by gravity and/or cohesive forces. Perrine et al. (2011) have added the ability to rigidly stick hard-sphere particles together in PKDGRAV, without the ability to bend or flex these bonds. In the newly adapted version of PKDGRAV presented in this paper, agglomerates of soft spheres bound together by spring-like forces that mimic their cohesion can be used to represent these bodies. In the study we present here, we use this newly adapted version of the code to represent material constructed in a real-world, Earth-based laboratory, and numerically calculate how this material reacts to the stresses of projectile impact and of confining pressure. Our results are then compared to the laboratory results. Our intention is not to particularly add to the interpretation of those results, but rather to demonstrate that we can reproduce them adequately as a first step toward developing a multi-purpose numerical tool.

A number of codes have already been developed in the general field of cohesive granular systems. For instance, Richefeu et al. (2009) used a 3-D discrete element method (DEM) with spherical particles enriched by a capillary force law to model the overall cohesion of wet granular materials. Also using a discrete element approach, Delenne et al. (2009) introduced a local cohesion law that accounts for the transition from capillary to cemented bonding in granular materials partially saturated with an aqueous solution. Then, Radjaï et al. (2010) treated the solid binding matrix filling (fully or partially) the interstitial space in a cohesive granular media by using a Lattice Element Method, which was based upon a lattice-type discretization of the particles and material matrix. More generally, different approaches are used to model granular materials. One approach is to treat the material as a continuum by averaging the physics across many particles. In the case of solid-like granular behavior, the continuum approach usually treats the material as elastic or elasto-plastic and models it with the finite element method or a mesh-free method (e.g., Elaskar et al., 2000; see also Holsapple (2004), Holsapple and Michel (2008), and Sharma et al. (2009) for use of analytical and continuum approaches in modeling asteroid shapes). However, the homogenization of granular-scale physics is not necessarily appropriate for capturing the discrete nature of the particles and the forces between them and between them and their wall-boundaries (Wada et al., 2006). Therefore, limits of such homogenization must be considered carefully before attempting to use a continuum approach. Discrete element numerical coding, on the other hand, is typically carried out by way of a hard-sphere or soft-sphere approach (termed the Hard- and Soft-Sphere Discrete Element Method, referred to as HSDEM and SSDEM, respectively, hereafter). In particular, SSDEM is commonly used in the study of granular materials, and has often been applied to industrial problems (Cleary and Sawley, 2002; Kosinski and Hoffmann, 2009; also see Radjaï and Dubois (2011) for a comprehensive overview). However, in comparison with the continuum approach, DEM is not well-suited to the treatment of supersonic motion, particle fragmentation, or phase-changing material. Within the appropriate regimes, which

are vast, only very recently has it started to be applied to the realm of planetary science. Granular physics codes are now developed or adapted specifically for planetary applications by various groups (e.g., Wada et al., 2006; Sánchez and Scheeres, 2011; Tancredi et al., 2012) using various integration schemes and implementations of the types of friction between grains. Other codes using a continuum approach (e.g., SPH hydroxides) have also been developed to investigate, for instance, collisions between porous aggregates (Sirono, 2004). The advantages and deficiencies between these codes and ours cannot be easily assessed, however the specifics of our newly adapted version of pkdgrav is that it uses a sophisticated tree-code to compute in parallel contact forces between particles along with self-gravity. In addition, a set of frictional forces, including static, dynamic, twisting, and rolling frictions has been introduced, all of which were not necessarily implemented or used in some of these mentioned codes.

In the following validation test of our numerical approach, we compare low-speed, laboratory impact experiments on glass bead agglomerates against simulations using the same impact conditions on numerical models of those targets. The impact experiments were performed in Japan at the Kobe University, the main results of which have been published by Machii and Nakamura (2011). In Section 2 we briefly present the experiments and the outcomes that we will consider in this paper for comparison with simulations. Section 3 briefly describes the numerical code PKDGRAV and its adaptation to address granular material physics and cohesion (see Schwartz et al. (2012) for details). Comparison between experiments and simulations are then presented in Section 4. Conclusions and perspectives are provided in Section 5.

2. Impact experiments

Machii and Nakamura (2011) performed their impact experiments on sintered glass bead agglomerates using a gas gun in Kobe University in Japan. Impact speeds ranged between 40 and 280 m/s and the sintered agglomerates used as targets contained ~40% porosity. Two kinds of targets were manufactured to differ in their bulk strength; the difference between the groups comes from the sintering times in the oven (8 h and 20 h). The size ratio of the beads to each target was 0.19, with the average bead size measuring ~5 mm in diameter. The experiments showed that the energy density required to catastrophically break the agglomerate is much less than that required for previously investigated sintered glass bead targets with the same porosity (e.g., Setoh et al., 2010). However, the sizes of the beads that comprised those targets and the size ratio of the beads to the targets were both 100 times smaller than the agglomerates used by Machii and Nakamura (2011). The authors suggest that this weaker strength is probably due to the much smaller number of cohesive links (necks) that a stress wave must travel through in this study, which minimizes the energy dissipation at the necks (this theory will be investigated and quantified in a future numerical study). Also, the fact that the particles are larger and less numerous enables them to move more freely and thus to be broken more easily. Catastrophic disruption of an agglomerate was shown to occur when the projectile kinetic energy was a few times the total energy needed to break all of the necks of the agglomerate. The distribution of fragment size and number was shown to be extremely dependent upon the impact point of the target.

3. Numerical method

3.1. The N-body code PKDGRAV: hard- and soft-sphere implementations

To model the targets and the impact experiment, we use the *N*-body code PKDGRAV, a parallel gravity code originally designed for

collisionless cosmology simulations (Stadel, 2001) and adapted for collisional Solar System applications (Richardson et al., 2000, 2009).

The original version of PKDGRAV only considered hard-sphere particles (HSDEM). In HSDEM, collisions are analytically predicted and treated as instantaneous, using coefficients of restitution to account for normal and tangential energy dissipation. The inclusion of walls of various geometries (boundaries) provides for the possible interaction of grains with experimental set-ups or small-body surfaces (see Richardson et al. (2011) for more details).

Recently, a Soft-Sphere Discrete Element Method was introduced in PKDGRAV (Schwartz et al., 2012), based initially on the work of Cundall and Strack (1979). In this case, collisions between spherical particles are not predicted in advance, and are not instantaneous. Instead, collisions are simulated by allowing particles to overlap with each other; to first order, this represents the slight surface deformation that occurs during the contact between real particles. When an overlap occurs, the various types of contact forces (e.g., static, dynamic, sliding, rolling frictions) are treated, and collisions are integrated through their full duration rather than analytically predicted in advance of the collision. This is particularly important in dense granular regimes and/or when collision durations (stress wave propagation speeds) are non-negligible. The reader is referred to Schwartz et al. (2012) for more details on the implementation of SSDEM in PKDGRAV and for a short review of other approaches to model these systems of granular materials.

3.2. Adding cohesion in PKDGRAV

In order to account for the potential presence of cohesion between grains within a granular medium such as regolith on the surfaces of solid celestial bodies, we have implemented a cohesive force into PKDGRAV. This added cohesive force acts between bonded particles' centers of mass (COMs) as a restoring force that opposes distention of the bond. Here we call the particle and the neighbor to which it is bound, particle 1 and particle 2, respectively.

A single bond is defined by an equilibrium separation $z(\epsilon,t)$ (a zero-strain-length) between the two particles' COMs, and a maximum strain $\epsilon_{max}(\dot{\epsilon})$ beyond which the bond has no effect, where the strain $\epsilon(t) \equiv [\rho/z] - 1$. We define $\boldsymbol{\rho} \equiv \mathbf{r}_2 - \mathbf{r}_1$ as the relative position between the particle and neighbor COMs, and so $\rho \equiv |\boldsymbol{\rho}|$ is the scalar distance between the COMs (thus, when $\rho = z(\epsilon,t)$, the length of the "spring" at rest, the strain, ϵ, vanishes). These variables are shown schematically as part of Fig. 1 (additional parameters that appear in the figure are introduced later in this section).

While $\epsilon(t) < \epsilon_{max}(\dot{\epsilon})$, a particle feels a cohesive force dependent upon the current strain $\epsilon(t)$, the current strain-rate $\dot{\epsilon}(t) \equiv \mathbf{u_n}/z(\epsilon,t)$, and the effective area of interaction A_{eff}, where $\mathbf{u} \equiv \mathbf{v_2} - \mathbf{v_1}$ is the relative velocity between the particle and neighbor to which it is bound, $\mathbf{u_n}$ is the normal component of this relative velocity.

We define the default behavior, which treats $\epsilon_{max}(\dot{\epsilon})$ as a constant $[\epsilon_{max}(\dot{\epsilon}) \rightarrow \epsilon_{max}]$, independent of the strain-rate, z as a constant independent of the effect of persistent strain $[z(\epsilon,t) \rightarrow z]$, and the force on the particle due to its attached neighbor as a linear combination of a strain (elastic) component and a strain-rate (plastic) component. We also require that cohesive bonds are to be broken once ϵ exceeds ϵ_{max}. We also take in default $A_{eff} \equiv \pi s_{eff}^2$, and $s_{eff} \equiv (s_1 + s_2)/2$, the mean radius of the particle and its neighbor. If we consider particles as effectively representing a continuum deformable agglomerate, this is an appropriate choice for the effective area of interaction, A_{eff}, especially for spheres of similar size. Although not the only option, this choice can also be justified for the area of interaction in the case of this study, when the spheres are treated as discrete particles and not a continuum (see Section 3.3).
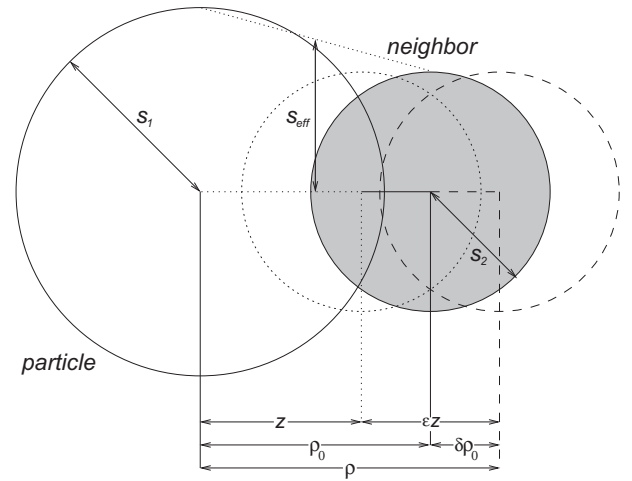
Fig. 1. A (spherical) particle in overlap with one of its neighbors. Both the particle and its neighbor feel an attractive force due to their cohesive bond and a repulsive SSDEM force (gravity is not considered in this figure). The shaded circle gives the relative position of the neighbor such that δ is zero, and thus these two forces cancel; therefore, the net force acting on the two particles is zero when ρ_0 describes the separation between their COMs, where δ is the fractional deviation of ρ from ρ_0. The dotted circle gives the relative position of the neighbor when the strain, ϵ, is zero, and thus the cohesive "spring" that forms the bond between the particles is at rest, which occurs at a separation of z. Here ρ gives the "current" separation between the particle and its neighbor, the latter inscribed by a dashed circle; thus in this case, they feel a net attractive force since $\rho > \rho_0$, which means that the cohesive force exceeds the SSDEM repulsive force. Here s_1 and s_2 are the radii of the particle and its neighbor, respectively, and s_{eff} we take to be the effective radius between them. When $\rho = s_1 + s_2 = 2s_{eff}, \epsilon = \epsilon_{max}$.

In this default configuration, from the time at which the bond is formed, up until the time at which ϵ exceeds ϵ_{max}, the force on a particle due to its cohesive bond (it may have multiple bonds), assuming implicit dependencies on t of the strain and the strain-rate, is given as

$$\mathbf{F_{1,coh}} = Y\epsilon A_{eff}\hat{\mathbf{n}} + \gamma z\dot{\epsilon}, \tag{1}$$

where $\hat{\mathbf{n}} \equiv \boldsymbol{\rho}/|\boldsymbol{\rho}|$ is a unit vector that gives the direction from the particle's center to the neighbor's center, Y is an elastic Young's modulus, and γ is a viscous damping term with the value for critical damping given as $\gamma_{crit} \equiv \sqrt{4\mu Y A_{eff}/z}$, with μ being the reduced mass of the two-particle system. Repulsive forces related to the cohesive bonds (for $\epsilon < 0$) can be switched on or off; we leave it off by default (this is not to be confused with the normal component of the SSDEM force, which always active). Newton's Third Law gives the force felt by the neighbor due to the cohesion with the particle as

$$\mathbf{F_{2,coh}} = -Y\epsilon A_{eff}\hat{\mathbf{n}} - \gamma z\dot{\epsilon}. \tag{2}$$

This treatment is equivalent to a Hooke's force law for springs with a speed-dependent damping term. Using the default implementation, as we do in this study, gives four parameters that define a cohesive bond: z, Y, ϵ_{max}, and γ. Also supported however, are more complicated force dependencies such as van der Waals force laws, a strain- and time-dependent zero-strain-length (creep), and cohesive strain limits that are dependent on strain rates. Although for the sake of this study, and for both simplicity and computational efficiency, we deliberately only approximate the actual cohesion physics using a simple model that nonetheless appears to capture the important experimental outcomes for our application.

In order to allow for more realistic (non-idealized) behavior of cohesive agglomerates, each cohesive element (particle–particle bond) has its own values for z, Y, and ϵ_{max}, where the distribution of strength (Y) and maximum strain (ϵ_{max}) are typically fit by a

gaussian distribution around specified mean values ($\langle Y \rangle$ and $\langle \epsilon_{\max} \rangle$).

Note also that these cohesive forces are central forces, and thus energy and momentum are conserved (although $\gamma > 0$ saps energy from the system). Forces are only applied along the line that connects the two particles' centers, thus there is no coupling with angular or tangential degrees of freedom.

3.3. SSDEM and cohesion

When the separation between the COMs of two bound particles is both greater than the sum of their radii, i.e., $\rho > s_1 + s_2$, and greater than z (with $0 < \epsilon < \epsilon_{\max}$), they feel a restoring force along the line that connects their two centers. However, in order to account for the existence of a physical neck that joins two sintered particles together (even if the atomic diffusion involved in the formation of the neck is not modeled explicitly), we must also consider coupling of translational and rotational degrees of freedom. This coupling would need also apply to the case of particles that feel mutual attraction through surface-surface interactions by way of van der Waals forces. However, this study does not model this type of cohesion, which requires a different prescription than the one used here. We describe in the following our strategy to couple translational and rotational degrees of freedom involving particles bound together with a physical neck that exists between them.

3.3.1. Building cohesive agglomerates

Setting $z < 2s_{\mathrm{eff}}$ implies that cohesive equilibrium occurs while particles are penetrating each others' surfaces. If we imagine a set-up of two mutually bound particles in isolation with zero-strain-length less than the sum of their radii, in HSDEM this amounts to the two particles pushing up against each other with some compressive force, but without ever penetrating (inter-particle penetration is not allowed in HSDEM). In SSDEM, this results in the particles penetrating each other with SSDEM repulsive forces coming into balance with cohesive forces and any force that may exist between the particles (e.g., gravity). In such a case, the particles' translational and rotational degrees of freedom are coupled. Furthermore, it means that particles are subject to the full robust treatment of SSDEM contact forces (Schwartz et al., 2012) together with cohesion. Including both elastic and plastic components, the net normal force on a particle as a result of its interaction with its neighbor, due to both cohesion and the SSDEM normal force is given as

$$\mathbf{F_1} = Y\epsilon A_{\mathrm{eff}}\hat{\mathbf{n}} + \gamma z\dot{\epsilon} - k_n x\hat{\mathbf{n}} + C_n\mathbf{u_n}, \tag{3}$$

where k_n is the SSDEM normal elastic coefficient given in units of kg/s^2, C_n is the SSDEM normal plastic coefficient given in kg/s (there also exist tangential analogues, k_t and C_t, respectively), and x is the amount of interparticle penetration as defined in Schwartz et al. (2012).

A number of studies have developed methodologies to allow for the representation of non-spherical shapes using ensembles of spherical particles (e.g., Gotteland et al., 2009; Azéma et al., 2012). Our approach also allows us to build up arbitrarily shaped objects consisting of spheres in various states of overlap with each other. The spheres need not be of uniform size or mass, and can have differing strength parameters, which provides us the freedom to simulate complex combinations of cohesive agglomerates with explicitly defined internal strength distributions. In this study, we use this approach to simulate individual particles bound together. Similarly, we have the ability to use a nearly identical approach for the simulation of a continuum solid, with each "particle" effectively acting as a tracer representing a section of the material.

In order to create the models for an object comprised of individual particles bound together, we must define, along with the SSDEM parameters, the COM position, the mass, and the radius for each particle of which it is comprised. Next, to account for cohesion within the object, we use pkdgrav's tree code and perform, for each particle, a search for other particles with which it is in overlap. For each of these overlaps, we assign a unique Young's modulus Y based upon our specification, and then solve for z such that the cohesive restoring force in Eq. (2) just cancels the SSDEM repulsive force when the object is at rest and in a state of internal equilibrium. We define ρ_0 for a pair of overlapping particles to be the separation between their centers when the net force between them is zero for the simulation at equilibrium at the start of the simulation (this is not to be confused with z, the separation between their centers when the cohesive force is zero—typically ρ_0 will be greater than z). The overlap value, $x = s_1 + s_2 - \rho_0$, gives:

$$z = \frac{\rho_0 Y A_{\mathrm{eff}}}{k_n(s_1 + s_2 - \rho_0) + Y A_{\mathrm{eff}}}. \tag{4}$$

Combining Eqs. (3) and (4), and defining $\delta \equiv [\rho/\rho_0] - 1$, for an unbroken bond where $z \leqslant \rho \leqslant 2s_{\mathrm{eff}}$, the force felt by a particle due to its interaction with its neighbor (ignoring gravity) reduces to:

$$\mathbf{F_1} = \delta[2k_n s_{\mathrm{eff}} + Y A_{\mathrm{eff}}]\hat{\mathbf{n}} + (\gamma + C_n)\mathbf{u_n}. \tag{5}$$

The fixed point at $\rho = \rho_0$ (when $\delta = 0$) can be seen in Eq. (5); when $\rho > \rho_0$, the elastic force on the particle pushes it toward its neighbor, and when $\rho < \rho_0$, the elastic force on the particle pushes it away from its neighbor, showing that the fixed point is stable (the diagram in Fig. 1 describes these lengths and dimensionless variables). Each particle that comprises these simulated cohesive objects exhibits this stable equilibrium with each of its neighbors (see Video 1). By default we set $\epsilon_{\max} = \frac{2s_{\mathrm{eff}}}{z} - 1$, breaking the bond between a pair of particles when they physically separate; this sets the tensile strength. The shear strength of the bond we set to be the static frictional force limit, such that the bond breaks when the tangential stress exceeds the product of the coefficient of static friction and the normal force (see Schwartz et al. (2012) for an outline of our treatment of static friction in SSDEM).

In this study, we use the default definition of A_{eff} as the mean cross-section of particles in contact. In reality, the contact area between sintered particles is smaller than the mean particle cross-section, especially for weakly sintered particles. However, to avoid unnecessary complexity, we keep A_{eff} constant so that we are able to control how the cohesion force depends on the strain, which in this study is taken to be linear. In principle, we could use other methods to set a constant A_{eff}, but as we will see in Section 4.1, this choice allows us to be consistent with the experimentally measured mean force that is required to break these bonds, which hold the agglomerates together.

When a bond is broken between a particle and its neighbor due to tangential stress, any future contacts between them are governed by standard SSDEM without cohesion. When a bond is broken due to shear stress, we must consider the consequence of losing the cohesive force while particles are still in overlap. Without special treatment, the SSDEM repulsive force would cause the particles to accelerate away from each other, which is not realistic behavior. Once their bond is broken, for the sake of future collisions, our approach is to allow particle pairs with broken bonds to see each other as spheres with contact radii equal to the distance from their respective centers to the contact point at the time of tangential failure of their bond. Under the assumption that collisions between formerly bound particles are likely to occur in similar orientations, this may be a fair approximation to make. For our purposes in this study, where re-colliding particles are not com-

mon or important to the outcome, this approximation should suffice.

4. Comparison between experiments and simulations

4.1. Numerical representation of the target

Our first task in this study is to use the above methodology to build a numerical representation of the target that is geometrically and mechanically as close as possible to the one used in experiments. The sizes of the real glass beads are large enough, and their shapes spherical enough, such that each bead can be represented by one spherical particle. The beads have been sintered, and the bonds between them measured. They are numerically modeled with cohesive strengths that correspond to the experimentally measured bonds.

Each 90-bead target was arranged in three layers of 30 beads, with the top and bottom layers arranged in the same, particular pattern. To construct the target, we start with its bottom layer (see Fig. 2): we first distribute the 16 particles that comprise the outside perimeter of this layer and then fill the inside with the remaining 14 particles. These 30 particles are placed on a horizontal plane, which is a boundary condition implemented in our numerical code (see Richardson et al., 2011). Indeed, such a boundary condition is necessary to maintain the configuration of those particles, when other ones will be distributed on top of them or in-

side them. Then, we distribute 16 particles on the outside perimeter of a second layer over the bottom one. We then attach elastic "springs" to all these 46 particles and then drop 14 particles inside to finish the second layer. Then, we model another horizontal plane slowly moving down onto those layers, in order to push particles into place. Once done, we remove this plane and add a third layer of 30 particles on the top of the two bottom layers in a similar way as previous layers. We numerically compute the motion of those three layers composed of 90 particles in total under uniform gravity to make them settle. Then we stop the simulations and make particles overlap with their neighbors by decreasing the distance between the centers of the particles by 10%, which means that the values for ρ_0 vary between bonds, but are typically $1.8s_{\text{eff}}$, or just under 4.5 mm.

The last step is to add cohesion to simulate the sintered particles. Each bond is characterized by a Young's modulus and a stress limit (equivalent to a tensile strength). The cohesive force between the glass beads of real targets is not perfectly identical for all bonds. In fact, quite a large variation exists between the strengths of the experimental bonds (see Fig. 4 in Machii and Nakamura (2011)). Given that some bonds in the real agglomerate are relatively quite weak and some relatively strong, it is important to represent this in our numerical model as it has a significant effect on how the sintered agglomerate breaks apart. Since there is no obvious way to determine the actual distribution of the bond strengths from the real target, in the modeled target, we arbitrarily distribute
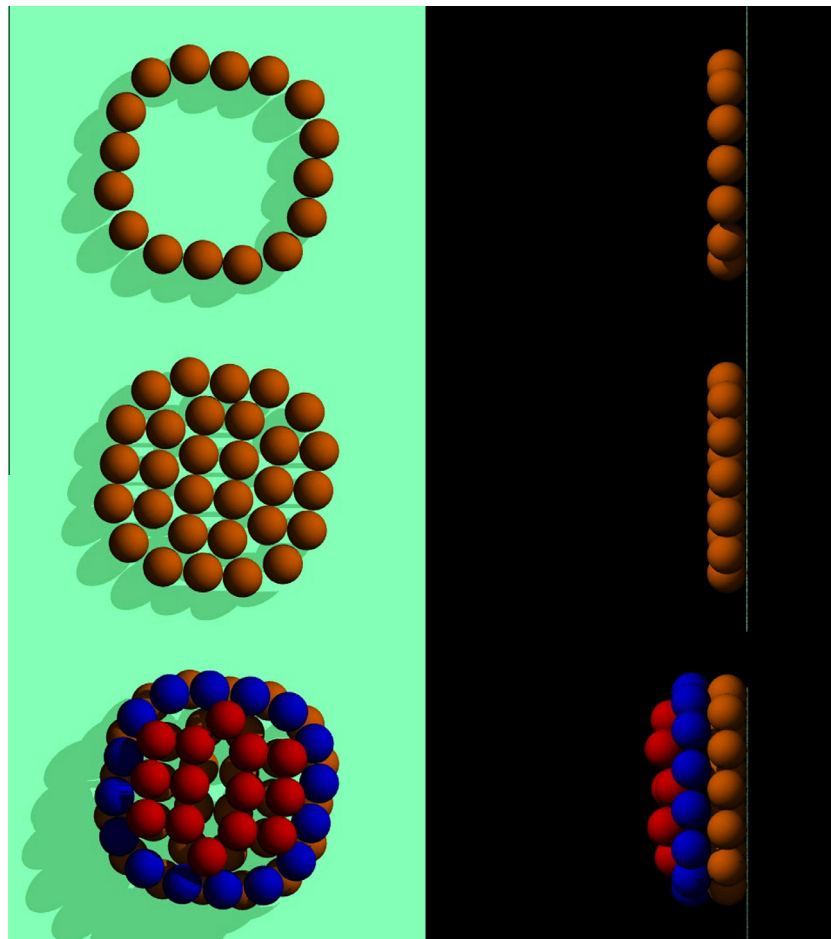
Fig. 2. Numerical construction of a modeled target. Top: first step in the modeling of the bottom particle layer placed on a horizontal plane. Middle: completed bottom layer. Bottom: modeling of the second layer over the bottom one. The process is repeated in a similar way for the rest of the target (see Fig. 3 for an image of the complete target). The left panel shows a top view while the right panel shows a side view. (Particle coloring/shading is used to distinguish the different phases in the fabrication process.) (For interpretation of the references to color in this figure legend, the reader is referred to the web version of this article.)

the values of the Young's modulus, Y, and stress limit to define the cohesion in the bonds according to truncated Gaussian distributions, with a mean of 4 ± 1 MPa and 1.59 ± 0.06 MPa, respectively. These values are based upon experimental bond strengths between individual pairs of sintered glass beads similar to those used to form the agglomerates (Machii and Nakamura, 2011). In this way we represent the fact that there is variation in the strengths of the bonds in the agglomerate. The stress limit is derived by assuming that the effective area of interaction, A_{eff}, is the entire cross section of a given particle, which is about 19 mm². In the experiments, the stress limit is indicated as around 6–10 MPa, considering the cross section of the fused area of contact of the particles, which is typically 2–5 mm². By taking the product of the stress limit with the particles' contact area, this means that it requires roughly the same force to break the bonds in the simulations as was required in the experiments, which is about 30 N. As we will see in Section 4.2, this allows us to obtain a bulk tensile strength that is similar to those measured experimentally. At the end of the process, our modeled 3-layer target is built with properties similar to the ones used in the laboratory experiments. Fig. 3 shows a comparison between a real target and a numerical one, using a ray tracer to make a realistic looking image.

4.2. Numerical modeling of the tensile strength measurement of the numerical target

Machii and Nakamura (2011) measured the tensile strengths of experimental targets using Brazilian disk tests. This test (first developed by Berenbaum and Brodie (1959)) is a common means of indirectly measuring the tensile strength of brittle materials, including rocks and concrete. In order to check that our numerical targets have a similar tensile strength as those used in experiments, we performed numerical simulations of Brazilian disk tests on our numerical targets.

Fig. 4 shows the numerical set up of the Brazilian disk test. The modeled target is placed between two flat plates, which are modeled as horizontal planes. These plates are set in motion towards each other until the target breaks into pieces. We modeled this test

using several strain rates: 0.1, 0.4, 1, 4 and 10 mm/s. The results are presented in Fig. 5 and show that the tensile strength slightly increases at higher strain rates. The tensile strength of the simulated target is comparable to those of the real ones constructed by Machii and Nakamura (2011); they all show significant variance around about 0.5 MPa.

4.3. Numerical simulations of impacts

In this section we present our numerical simulations aimed at reproducing the impact experiments of Machii and Nakamura (2011). The experiments led to a wide range of outcomes depending on the initial conditions. Some impacts did not break the target, while others led to the shattering of individual beads. For our modeling we considered two experiments that led to the fragmentation of the target without any shattering of individual beads, so that the full process can be captured in principle with our numerical code.

The two considered experiments were performed using different projectiles and impact speeds. Both involve the stronger targets, fused for 20 h, because those involving the weaker targets showed much more scatter in their results. The first considered experiment involves a projectile consisting of an individual 3.07 mm glass bead impacting the target at 78 m/s, which corresponds to a specific impact energy, defined as the kinetic energy of the projectile divided by the target mass, of 8.95 J/kg. The second experiment involves a 2.85 mm individual glass bead impacting the target at 56 m/s, which corresponds to a specific impact energy of 4.29 J/kg. The projectile hit close to the target's center in each case. However, because the exact location of the impact point could not be measured, and given the sensitivity of the outcome on the exact impact point location, we performed a suite of simulations, varying the impact point position around the target's center. Although we were able to satisfactorily reproduce both experiments, we report in greater detail only the case of the 78 m/s impactor.

In order to study the case of the 78 m/s impactor, we randomly assigned 28 impact points all lying within a one-bead-diameter by
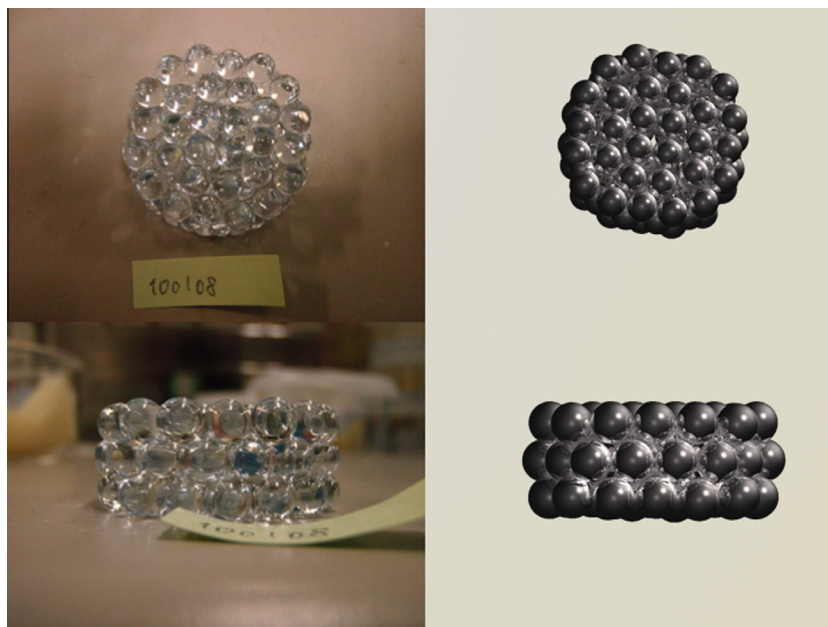
Fig. 3. Left: experimental target consisting of a sintered glass bead agglomerate. Right: modeled target consisting of soft spheres bound together by cohesive forces. Top and side views are shown.
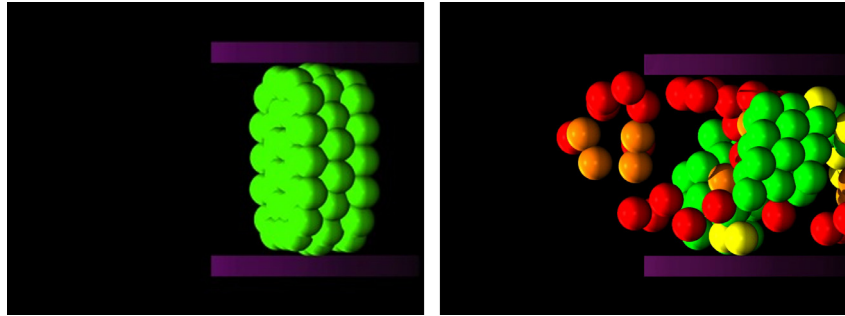
Fig. 4. Numerical set up and simulation of the Brazilian disk test. Left: the target is placed between two horizontal planes that move vertically towards the center of the target until it breaks. Right: snapshot of the simulation at a time when the target is broken as its tensile strength is reached. The target is broken from its center into two main pieces, and other smaller ones. (Online only: particles in green are bound to three or more other particles, particles in yellow to two other particles, particles in orange to one other particle, and particles in red are unbound.) (For interpretation of the references to color in this figure legend, the reader is referred to the web version of this article.)
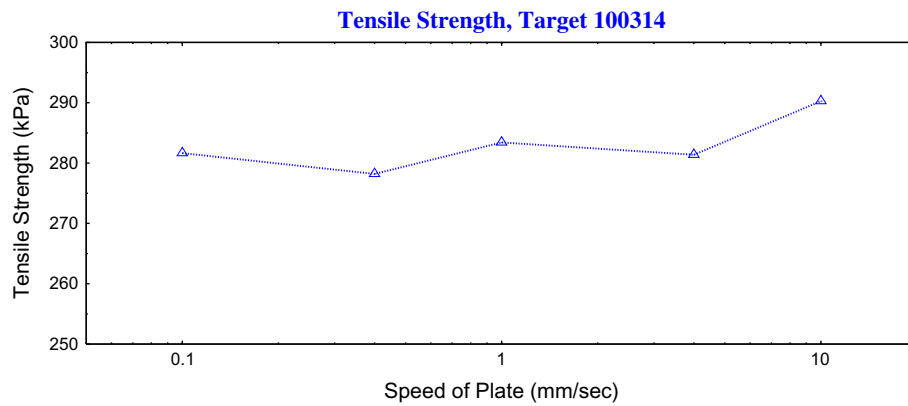
Fig. 5. Tensile strength (kPa) of the modeled target as a function of the speed of the plates between which it is placed in the simulated Brazilian disk tests.
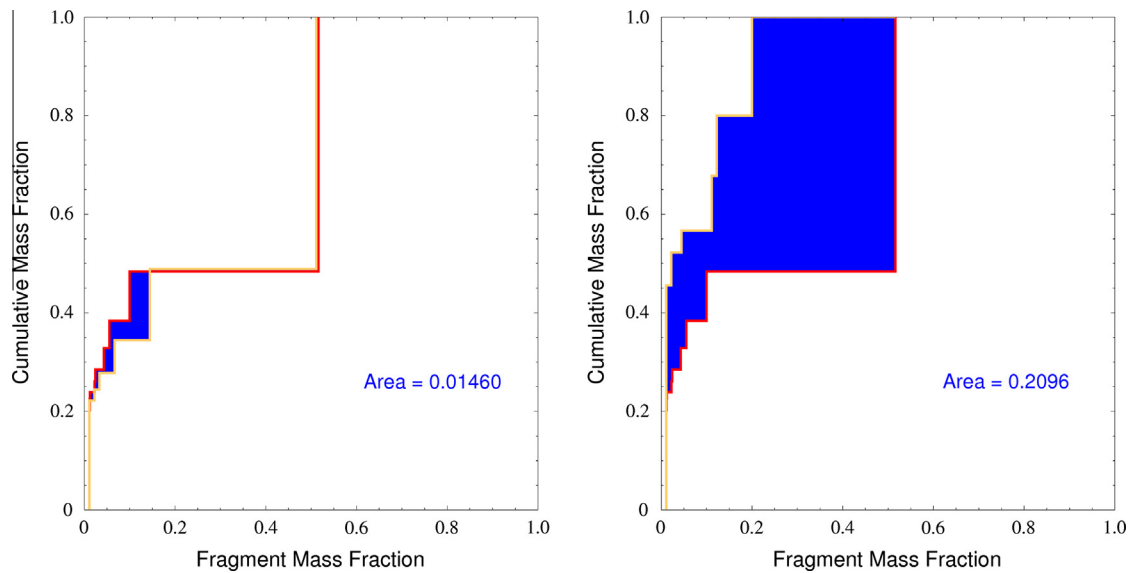
Fig. 6. Cumulative mass distributions of fragments from both the 3.07 mm-diameter, 78 m/s projectile impact experiment (red line/small dashes) and simulation (yellow line/large circles). Left: Of the 1008 simulations run to represent this experiment, the simulation whose fragment mass distribution curve is closest to the curve corresponding to the experiment (represented on the top row of Table 2) is shown. Right: A simulation whose fragment mass distribution curve differs more significantly from that of the experiment. (For interpretation of the references to color in this figure legend, the reader is referred to the web version of this article.)

one-bead-diameter rectangular region (0.24 cm²), centered at the target's center. Each of the two plots in Fig. 6 show the mass histograms of fragments from the experiment along with the mass histogram from a particular simulation. The difference of the two distribution functions from that of the experiment is quantified by an area, which characterizes the extent of the disagreement between the given simulated result and the experimental result. This area is given by:

$$A = \int_{m_f=0}^{m_f=1} |\mathscr{F}(m_f) - \mathscr{G}(m_f)|, \qquad (6)$$

where m_f is the mass fraction of the fragment, and $\mathscr{F}(m_f)$ and $\mathscr{G}(m_f)$ are the cumulative mass distribution functions representing the final fragment sizes from the simulation and the experiment, respectively. A lower value of A represents a better match to the experiment. Upon first glance, a Kolmogorov–Smirnov test (K–S test) seems like the appropriate statistic to quantify by how much the datasets from the simulation differ from that of the experiment. However, because the fragment sizes are in integer units of beads, and for the simulations that fit best most fragments are in fact single beads, there is limited discriminatory power. This experiment had 27 fragments of which only 6 were comprised of more than one bead, which is not enough to distinguish well between the distributions using a K–S test. As an alternative, we try to match the number of single bead fragments and the sizes of the larger fragments by overlaying the histograms and quantifying the area between them. Using this measure, as well as confirming with visual qualitative comparisons between the actual and simulated impact animations, we assess the relative quality of the fit.

For each of the 28 impact points, given in Table 1 and shown graphically in Fig. 7, we simulated 36 impacts, with target SSDEM parameters varied around a region of parameter space where the results from the simulations were close to the experimental results. The "fidelity fit parameter" A from each of the 36 sets of parameters is averaged together, and is also shown in the aforementioned table and figure. The same values of k_n, C_n, k_t, and C_t were used for each simulation—these are 5.91×10^4 kg/s^2; 1.16 kg/s for interacting target particles chosen to correspond to a normal coefficient of restitution of 0.4; 1.69×10^4 kg/s^2; and 1.30 kg/s for interacting target particles, respectively. We chose a value of k_n that would balance several considerations: we wanted particles in the agglomerate to have a proper amount of overlap, for their bonds to have the correct Young's modulus and the correct range in tensile force required to break the bonds, and also that the amount of overlap experienced during collisions is reasonable. There is no consensus about the correct values to use for k_t; we chose to keep it fixed at $2/7\ k_n$, which was suggested as a sensible choice by Silbert et al. (2001), and Schwartz et al. (2012) shows that a factor of $2/7$ relates the oscillation frequencies of the normal and tangential springs of soft spheres in contact.

The parameters that were varied were the coefficients of static, rolling, and twisting friction, μ_s, μ_r, and μ_t, respectively (see Table 2 for the best fit values). We find that outcomes were sometimes
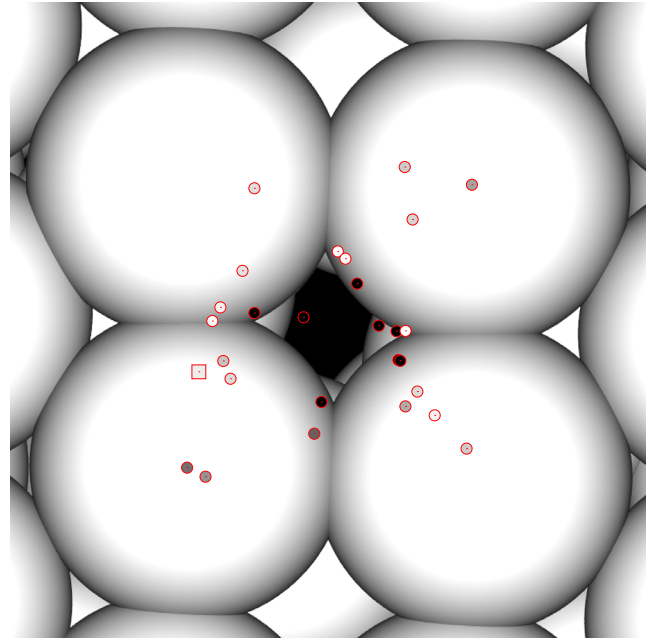
Fig. 7. Image of the central region of the target, overlaid with the 28 randomly selected impact points used to simulate the 3.07 mm-diameter, 78 m/s projectile impact experiment. Shading shows the quality of the fit, from darkest (worst fit) to lightest (best fit) as measured by the fidelity parameter A as defined in the text, averaged over all 36 shots at the given location. Twelve of the 17 best-fitting simulations, including the top five simulations, came from just one of these impact points, indicated with a square (see Table 2).

quite different between simulations where one of these parameters differed only slightly. However, much more important in determining the outcome of a simulated impact was the precise point of impact on the target. Table 2 shows the 17 best fits, in order, beginning with the best fit as quantified by its A value. It is worth noting that 12 of these come from a single impact point, highlighting the dependency of outcome on the precise point of impact. The histogram from the best fit derived from the criterion given in Eq. (6) is also shown in Fig. 6 (left image), overlaid with the experimental histogram.

For one of the impact points, we also performed two similar simulations using different compilers of the code. The rationale for testing different compilers is that such dynamical systems are

Table 1

Simulation impact conditions for the first considered experiment. In each case, the projectile mass is 0.0382 g, its diameter is 3.07 mm, and the impact speed is 78 m/s. The impact points are randomly chosen to be within one target-bead radius of the target's center in each the horizontal and vertical dimensions, with the offset from the target's center given as X-offset and Y-offset, respectively. The last column of the table gives the derived fidelity parameter, A, which is a measure of the goodness of fit relative to the experiment (Eq. (6)), averaged over each of the 36 shots at this location. The table is ordered by increasing $\langle A \rangle$, with smaller values of $\langle A \rangle$ implying a better match to the experiment.

X-offset (mm)	Y-offset (mm)	$\langle A \rangle$	X-offset (mm)	Y-offset (mm)	$\langle A \rangle$
0.506856	3.54584	0.110412	−5.4794	−2.18385	0.175271
4.04949	−0.611243	0.111942	4.04424	−4.56093	0.201764
−6.05097	−0.0956444	0.113853	7.5203	7.03134	0.214827
0.906545	3.16675	0.11974	−6.40953	−8.23685	0.229588
5.57488	−5.02434	0.123184	−7.37184	−7.76246	0.270061
−5.63123	0.618798	0.124316	−0.721407	−5.98887	0.286138
−6.75735	−2.75084	0.131877	−1.28281	0.0986582	0.714857
−4.47548	2.53149	0.142	1.51821	1.8634	0.714857
−3.85291	6.84779	0.148301	2.65272	−0.337877	0.714857
4.67133	−3.78316	0.149337	3.58045	−0.630038	0.714857
−5.10094	−3.11317	0.150283	3.6803	−2.13386	0.714857
4.4179	5.21704	0.158512	3.77577	−2.17328	0.714857
4.00789	7.96096	0.167667	−3.85397	0.328069	0.714857
7.24145	−6.76692	0.168172	−0.347942	−4.32904	0.714857

Table 2
Best-fit simulation impact conditions for the first considered experiment as given by the fidelity fit parameter A (shown). The SSDEM parameters of static friction, rolling friction, and twisting friction, are represented by μ_s, μ_r, μ_t, respectively. The mass of the largest remnant relative to the target mass is indicated by M_{lr}/M_t. From the first experiment, the value of M_{lr}/M_t was 0.516.

X-offset (mm)	Y-offset (mm)	μ_s	μ_r	μ_t	M_{lr}/M_t	A
−6.75735	−2.75084	0.141	0.1	0.05	0.511	0.01460
−6.75735	−2.75084	0.14	0.1	0.02	0.511	0.01691
−6.75735	−2.75084	0.143	0.1	0.05	0.511	0.01740
−6.75735	−2.75084	0.141	0.15	0.02	0.511	0.01790
−6.75735	−2.75084	0.148	0.2	0.02	0.533	0.02200
−5.4794	−2.18385	0.145	0.1	0.02	0.522	0.02375
−6.75735	−2.75084	0.142	0.1	0.05	0.489	0.02694
−5.4794	−2.18385	0.144	0.1	0.02	0.489	0.02743
−6.75735	−2.75084	0.147	0.2	0.02	0.489	0.02843
4.04949	−0.611243	0.148	0.1	0.02	0.522	0.04031
−4.47548	2.53149	0.145	0.1	0.02	0.522	0.04031
−6.75735	−2.75084	0.143	0.1	0.02	0.544	0.04573
−6.75735	−2.75084	0.145	0.1	0.02	0.533	0.05015
−6.75735	−2.75084	0.146	0.1	0.02	0.544	0.05042
4.47548	2.53149	0.147	0.1	0.02	0.478	0.05119
−6.75735	−2.75084	0.146	0.15	0.02	0.567	0.05346
−6.75735	−2.75084	0.147	0.1	0.02	0.544	0.05437

not purely deterministic, and can often be very sensitive to the different round-off and truncation errors that result from the use of different compilers and computer architectures. Here, we found that results remained nearly the same.

In our simulations of the other experiment, which used the 2.85 mm projectile moving at 56 m/s, we found that using the values of 0.144, 0.2, and 0.2 for μ_s, μ_r, and μ_t, respectively, coupled with a specific impact point best replicated the impact. Fig. 8 shows the mass histogram of fragments from the simulation imposed on top of the corresponding mass histogram from the experiment.
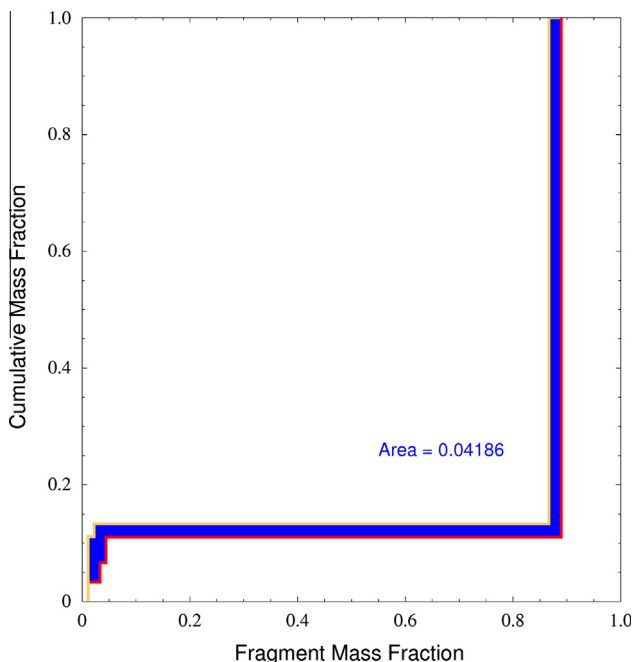
Fig. 8. Cumulative mass distribution of fragments from the 2.85 mm-diameter, 56 m/s projectile impact experiment (red line/small dashes) and best-fitting simulation (yellow line/large circles). (For interpretation of the references to color in this figure legend, the reader is referred to the web version of this article.)

5. Conclusions and perspectives

In this paper, we investigated the ability of our implementation of cohesion and SSDEM in the numerical *N*-body code `pkdgrav` to reproduce low-speed impact experiments on targets composed of 90 large glass beads sintered together carried out at the Kobe University in Japan (Machii and Nakamura, 2011).

First, we numerically reproduced the targets that were used in the experiments, and checked that they had similar properties, the tensile strength in particular. To do this, we performed a simulated Brazilian disk test, on the numerical targets. This test consists of placing the target between two converging horizontal plates and measuring the stress at which the target breaks. The tensile strength of the numerical target measured in simulation was commensurate with the tensile strengths of similar targets measured in the lab.

Then, we performed suites of simulations to represent two different impact experiments by sweeping the parameter space around reasonable values. We developed a quantitative argument for why some simulations match the experiments better than others and found that the outcome is sensitive to the exact location of the impact point on the target, as was observed in the experiments. For each experiment, we compared qualitatively the outcomes of the simulations by overlaying the histogram of a given simulation to that of the experiment and measuring the area between the two; we found reasonable matches for many simulations. Because of the difficulty involved in measuring the velocity distributions of fragments from the images, the fragment-size distribution is really the best measure of the simulation fidelity to the experiments. We also confirmed, by visually rendering the simulations, the similarity in the fragmentation process and the realistic motion of the ejecta fragments. We compared the simulations to snapshots of the fragmentation process at different instances and assessed that the degree of spreading of the fragments in space was essentially the same in experiment and simulation. By selecting for similarity in the histograms and a careful visual inspection of the post-impact evolution of the fragments, we feel confident that we have produced multiple good simulations of both impact experiments, and that the outcome is strongly influenced by the precise point of impact.

We thus performed a satisfying validation test of our implementation of cohesion and SSDEM for these kinds of processes. The understanding of impacts on cohesive targets that do not involve the fragmentation of individual components can be important in the context of planetary formation. This is especially the case in the phase when collisional speeds are low and small particles aggregate. In future studies, we plan to investigate this process in more detail by covering a wider range of parameter space (e.g., cohesion, friction coefficients, etc.), and using targets of various shapes and/or composed of spheres of different sizes and investigating the effect of initial target rotation. We will also apply our numerical method to the process of YORP spin-up on asteroids modeled as cohesive aggregates using as a basis the work performed with `pkdgrav`'s HSDEM collision routine by Walsh et al. (2008, 2012) for purely gravitational aggregates.

Appendix A. Supplementary material

Supplementary data associated with this article can be found, in the online version, at http://dx.doi.org/10.1016/j.icarus.2013.05.007.

References

Azéma, E., Estrada, N., Radjaï, F., 2012. Nonlinear effects of particle shape angularity in sheared granular media. Phys. Rev. E. 86, 041301-1–041301-15.

Benz, W., Asphaug, E., 1999. Catastrophic disruptions revisited. Icarus. 142, 5–20.

Berenbaum, R., Brodie, I., 1959. Measurement of the tensile strength of brittle materials. Br. J. Appl. Phys. 10 (6), 281–287.

Cleary, P.W., Sawley, M.L., 2002. DEM modelling of industrial granular flows: 3D case studies and the effect of particle shape on hopper discharge. Appl. Math. Model. 26, 89–111.

Consolmagno, G.J., Britt, D.T., Mackeb, R.J., 2008. The significance of meteorite density and porosity. Chemie der Erde – Geochemistry 68, 1.

Cundall, P.A., Strack, O.D.L., 1979. A discrete numerical model for granular assemblies. Geotechnique 29, 47–65.

Delenne, J.-Y., Soulié, F., El Youssoufi, M.S., Radjaï, F., 2009. A numerical model for transition from liquid to solid bonding in cohesive granular media. AIP Conf. Proc. 1145, 893–896.

Elaskar, S.A., Godoy, L.A., Gray, D.D., Stiles, J.M., 2000. A viscoplastic approach to model the flow of granular solids. Int. J. Solids Struct. 37, 2185–2214.

Gotteland, P., Villard, P., Salot, C., 2009. Using nonconvex discrete elements to predict experimental behaviour of granular materials. AIP Conf. Proc. 1145, 361–364.

Holsapple, K.A., 2004. Equilibrium figures of spinning bodies with self-gravity. Icarus 172, 272–303.

Holsapple, K.A., 2007. Spin limits of Solar System bodies: From the small fast-rotators to 2003 EL61. Icarus 187, 500–509.

Holsapple, K.A., Michel, P., 2008. Tidal disruptions. II. A continuum theory for solid bodies with strength, with applications to the Solar System. Icarus 193, 283–301.

Kosinski, P., Hoffmann, A.C., 2009. Extension of the hard-sphere particle–wall collision model to account for particle deposition. Phys. Rev. E. 79, 061302-1–061302-11.

Machii, N., Nakamura, A.M., 2011. Experimental study on static and impact strength of sintered agglomerates. Icarus 211, 885–893.

Perrine, R.P., Richardson, D.C., Scheeres, D.J., 2011. A numerical model of cohesion in planetary rings. Icarus 212 (2), 719–735.

Radjaï, F., Dubois, F., 2011. Discrete-Element Modeling of Granular Materials. Wiley-Iste, Berlin, 425pp. ISBN 978-1-84821-260-2.

Radjaï, F. et al., 2010. Force transmission in cohesive granular media. AIP Conf. Proc. 1227, 240–259.

Richardson, D.C., Quinn, T., Stadel, J., Lake, G., 2000. Direct large-scale N-body simulations of planetesimal dynamics. Icarus 143, 45–59.

Richardson, D.C., Michel, P., Walsh, K.J., Flynn, K.W., 2009. Numerical simulations of asteroids modeled as gravitational aggregates. Planet. Space Sci. 57, 183–192.

Richardson, D.C., Walsh, K.J., Murdoch, N., Michel, P., 2011. Numerical simulations of granular dynamics: I. Hard-sphere discrete element method and tests. Icarus 212, 427–437.

Richefeu, V., Radjaï, F., El Youssoufi, M.S., 2009. Shear strength and stress distribution in wet granular media. AIP Conf. Proc. 1145, 919–922.

Sánchez, P., Scheeres, D.J., 2011. Simulating asteroid rubble piles with a self-gravitating soft-sphere distinct element method model. Astrophys. J. 727 (120), 14 pp.

Schwartz, S.R., Richardson, D.C., Michel, P., 2012. An implementation of the soft-sphere discrete element method in a high-performance parallel gravity tree-code. Granul. Matter 14, 363–380.

Setoh, M., Nakamura, A.M., Michel, P., Hiraoka, K., Yamashita, Y., Hasegawa, S., Onose, N., Okudaira, K., 2010. High- and low-velocity impact experiments on porous sintered glass bead targets of different compressive strengths: Outcome sensitivity and scaling. Icarus 205, 702–711.

Sharma, I., Jenkins, J.T., Burns, J.A., 2009. Dynamical passage to approximate equilibrium shapes for spinning, gravitating rubble asteroids. Icarus 200, 304–322.

Silbert, L.E., Ertas, D., Grest, G.S., Halsey, T.C., Levine, D., Plimpton, S.J., 2001. Granular flow down an inclined plane: Bagnold scaling and rheology. Phys. Rev. E. 64, 051302-1–051302-14.

Sirono, S., 2004. Conditions for collisional growth of a grain aggregate. Icarus 167, 431–452.

Stadel, J., 2001. Cosmological N-Body Simulations and Their Analysis. Thesis, University of Washington, Seattle. 126pp.

Tancredi, G., Maciel, A., Heredia, L., Richeri, P., Nesmachnow, S., 2012. Granular physics in low-gravity environments using discrete element method. Mon. Not. R. Astron. Soc. 420, 3368–3380.

Wada, K., Senshu, H., Matsui, T., 2006. Numerical simulation of impact cratering on granular material. Icarus 180, 528–545.

Walsh, K.J., Richardson, D.C., Michel, P., 2008. Rotational breakup as the origin of small binary asteroids. Nature 454, 188–191.

Walsh, K.J., Richardson, D.C., Michel, P., 2012. Spin-up of rubble-pile asteroids: Disruption, satellite formation, and equilibrium shapes. Icarus 220, 514–529.

Yeomans, D.K. et al., 1997. Estimating the mass of Asteroid 253 Mathilde from tracking data during the NEAR flyby. Science 278, 2106–2109.